Simulating the galvanic coupling between S-Al_2CuMg phase particles and the matrix of 2024 aerospace aluminium alloy

L. Lacroix [a,*], C. Blanc [a], N. Pébère [a], G.E. Thompson [b], B. Tribollet [c], V. Vivier [c]

[a] Université de Toulouse, CIRIMAT, UPS/INPT/CNRS, ENSIACET, 4, allée Emile Monso, BP 44362, 31030 Toulouse cedex 04, France
[b] Corrosion and Protection Centre, School of Materials, The University of Manchester, Manchester M13 9PL, England, UK
[c] Laboratoire Interfaces et Systèmes Electrochimiques, UPR 15 du CNRS, Université Pierre et Marie Curie, 4, Place Jussieu, 75252 Paris cedex 05, France

A B S T R A C T

Study of the corrosion behaviour of a magnetron sputtered Al–Cu/Al–Cu–Mg model alloy couple in sulphate solutions has been undertaken to gain insight into the galvanic coupling between the matrix and S-Al_2CuMg particles in the 2024 aluminium alloy (AA2024). Polarisation curves and local electrochemical impedance spectroscopy measurements (LEIS) were performed on the individual alloys and on the model alloy couple. SEM enabled correlation of electrochemical phenomena to the observed damage. The corrosion behaviour of the sputtered alloys was shown to be representative of the AA2024, with the Al–Cu–Mg alloy part undergoing localised corrosion and the Al–Cu alloy part remaining passive.

Keywords:
A. Aluminium
A. Sputtered films
B. Polarisation
B. LEIS
C. Galvanic coupling

1. Introduction

2024 Aluminium alloy (AA2024) remains important for aerospace applications due to the high strength-to-weight ratio and damage tolerance. However, this alloy is susceptible to corrosion and, specifically, to intergranular corrosion which has been studied extensively [1–7]. The corrosion susceptibility of the AA2024 alloy is known to be due to the heterogeneous microstructure of the alloy, which is a consequence of the thermomechanical processing history. S-Al_2CuMg particles are one of the coarse, primary intermetallic particles associated with the AA2024 alloy system, and their reactivity and tendency to constitute preferential initiation sites for corrosion have been widely investigated [8–14]. However, such mechanisms of intermetallic dissolution continue to be discussed. In order to explain the observed corrosion phenomena, galvanic coupling between the particles and the surrounding matrix are considered.

To study these phenomena, local techniques [14–18] such as atomic force microscopy (AFM) combined with scanning Kelvin probe force microscopy (SKPFM) are often used [16–18]. These local techniques provide high lateral resolution, which is often lacking in conventional electrochemical approaches. Other authors have studied the corrosion behaviour of model alloys representative of the different metallurgical phases [19–21]. Several mechanisms have been suggested for S-phase dissolution in the AA2024 alloy [8,10,12,13,18,22]. A two-step mechanism has been proposed that consists of preferential dissolution of aluminium and magnesium (*Step 1*), with the intermetallic particles acting as anodes and generating copper-enriched particles after some immersion time, the copper-enriched particles switch to a cathodic behaviour (*Step 2*) [18]. In order to reproduce separately these two steps, simple systems such as a pure aluminium/pure magnesium couple (representative of the first step) and a pure aluminium/pure copper couple (representative of the second step) have been recently studied [23,24]. Both systems were examined with physical contact between the two materials of the couple, and were demonstrated to be appropriate for understanding the corrosion mechanisms associated with copper- and magnesium-rich intermetallics in Al–Cu–Mg alloys.

In the present study, an Al–Cu model alloy representative of the α-Al AA2024 matrix and an Al–Cu–Mg model alloy representative the S-Al_2CuMg phase were synthesised by magnetron sputtering to simulate the corrosion behaviour of the AA2024. Such thin film model alloys have been shown previously to give relevant data on the electrochemical behaviour of the metallurgical phases represented [25–27]. The present paper is focussed on macroscopic (open circuit measurements and polarisation curves) and local (local electrochemical impedance spectroscopy) techniques to study the electrochemical behaviour of each individual model alloys and of the couple. In the first step, the corrosion behaviour of each individual model alloy was studied using potentiodynamic polari-

* Corresponding author. Address: Université de Toulouse, LGP, ENIT, 47 av. d'Azereix, BP 1629, 65016 Tarbes Cedex, France. Tel.: +33 5 62 44 27 23; fax: +33 5 62 44 27 08.
E-mail address: loic.lacroix@enit.fr (L. Lacroix).

http://dx.doi.org/10.1016/j.corsci.2012.07.020

sation. In the second step, interpretation of the model couple behaviour was assisted by local electrochemical impedance spectroscopy (LEIS).

2. Experimental

2.1. Material and systems

The model alloys consisted of thin films sputtered on electropolished aluminium substrates. The alloys were synthesised using an Atom Tech DC magnetron sputtering system with provision for 50 mm diameter targets. In the present case, aluminium (99.99%), copper (99.95%) and magnesium (99.95%) targets were used. The substrates were placed on a large copper disk (300 mm diameter), which was rotated at 250 rpm to ensure composition and thickness uniformity of the alloys. The deposition was performed at room temperature. After evacuating to 6×10^{-7} mbar, deposition was performed at 5.5×10^{-3} mbar in 99.998% argon at room temperature. Three types of material were synthesised, namely the individual Al–Cu alloy, the individual Al–Cu–Mg alloy and the couple of both alloys. Concerning the Al–Cu model alloy, it was synthesised to be representative of the AA2024 matrix. The AA2024 matrix was considered as the α-Al solid solution containing the hardening precipitation (mostly GPB zones) and dispersoids. It contains aluminium and copper but also other alloying elements. However, in this study, the only alloying element considered was copper and the composition of the Al–Cu model alloy expected was around Al–2.8 at.%Cu i.e. Al–4 wt.%Cu. Al–Cu–Mg model alloys were synthesised to be chemically representative of the S-phase particles with an expected composition of Al–25 at.%Cu–25 at.%Mg. As described in Fig. 1, to synthesise the model couple, the Al–Cu model alloy was first deposited on an electropolished aluminium substrate. Then, a mask was placed on the sample to cover a part of the surface and the Al–Cu–Mg model alloy was subsequently deposited. Finally, the mask was removed. A surface area ratio of 1:1 between both components of the couple was obtained. No surface preparation was performed on the specimens before the electrochemical studies.

2.2. Electrochemical measurements

The corrosion behaviour of the model alloys and the coupled system was studied in sulphate solutions at room temperature with the electrolyte in contact with air. The electrolytes were 10^{-1} M Na_2SO_4 and 10^{-3} M Na_2SO_4 solutions, and were prepared from analytical reagent grade chemicals dissolved in distiled water (pH values between 6 and 7). The specimen electrodes (Fig. 1) were prepared by connecting the substrates, on which the model alloys were deposited, to an electric wire using silver paint, then pasting them on a plastic support with epoxy resin and isolating the electric connection from the electrolyte using epoxy resin. Care was taken in electrode preparation to ensure artifacts were not introduced, i.e. galvanic couples, and to ensure only the model alloy was exposed to the electrolyte. The OCP measurements consisted of recording the free corrosion potential during immersion. In the following, all potentials are given with respect to the mercury/mercurous sulphate electrode (MSE), with saturated potassium sulphate solution (+0.65 V vs. SHE, the Standard Hydrogen Electrode, at 25 °C). Polarisation curves were recorded after immersion for 10 min when the corrosion potential was relatively stable. The potential was scanned from the cathodic domain (−1.4 V/MSE) to the anodic domain (+0.6 V/MSE) with a 1 V/h potential scan rate. Local electrochemical impedance spectroscopy (LEIS) was performed with a Solartron 1275 system, using a five-electrode configuration [28–30]. The probe (i.e. a bi-electrode allowing local current density measurement) was stepped across selected points of the sample. The analyses were performed in the centres of the individual model alloys and along a line perpendicular to the Al–Cu/Al–Cu–Mg interface of the model alloy couple. The LEIS measurements were performed in a frequency range of 3 kHz–100 mHz with eight points per decade using 20 mV peak-to-peak sinusoidal potential. With the experimental set up employed, only the normal component of the current was measured.

2.3. Optical and chemical characterisations

The samples were observed prior to immersion and after immersion for 600 min in 10^{-3} M Na_2SO_4 solution with an Olympus PMG3 microscope; *in situ* observations were also performed. Energy dispersive X-ray spectroscopy (EDS) was used for elemental analysis, employing a JEOL-JEM-2010 transmission electron microscope (TEM) and a Leo 435VP scanning electron microscope (SEM). The EDS analysis was performed at an electron beam accelerating voltage of 5 keV in order to reduce the electron interaction volume and to localise the chemical analysis within the model alloy layer.

3. Results and discussion

3.1. Structure and composition of the model alloys before corrosion tests

The model alloy microstructure was characterised by transmission electron microscopy (TEM), with Fig. 2 showing a micrograph of the Al–Cu alloy (Fig. 2a) and the corresponding electron

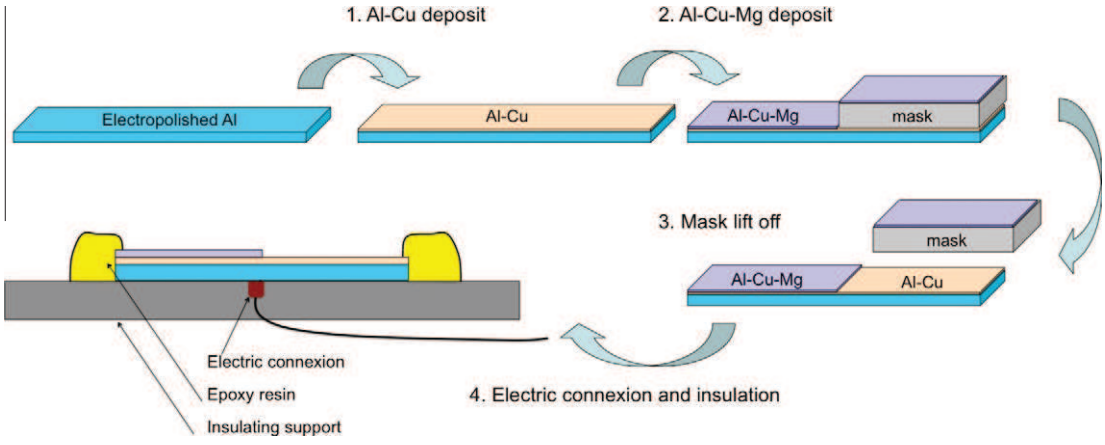

Fig. 1. Schematic representation of the realisation steps of a Al–Cu–Mg/Al–Cu model couple electrode.

diffraction pattern (Fig. 2b). The Al–Cu alloy was relatively uniform in thickness (about 450 nm thick) and free of defects that may expose the underlying aluminium substrate to the electrolyte. Such model alloys are suitable for electrochemical tests with no risk of galvanic coupling with the aluminium substrate. A typical polycrystalline structure was observed for the Al–Cu alloy, which was assumed to be representative of the α-Al AA2024 matrix. It was confirmed by electron diffraction (Fig. 2b). The diffraction spots are indeed characteristic of a crystalline aluminium structure. Concerning Al–Cu model alloys, equilibrium phase diagram showed that, for a copper content of 4 wt.%, both α-Al and θ-Al_2Cu phases are to be observed. However, Idrac et al. showed that, for a copper content less than 5 at.%, magnetron sputtered Al–Cu model alloys are composed of α-Al supersaturated solid solution with very little or no θ-Al_2Cu phase [25,27], which is representative of the AA2024 matrix. In the present study, two kinds of grains are distinguished, namely fine equiaxed grains at the interface between the aluminium substrate and the sputtered alloy (grains marked 1–5 in Fig. 2a, the diameter of which are about 50 nm), and columnar grains that transverse the remaining alloy thickness (grains 6–13 in Fig. 2a). EDS analyses at the numbered locations were also performed, with the elemental analyses given in Tables 1 and 2. The equiaxed grains, located at the inner part of the deposit, revealed a mean copper content around 24 at.%Cu, less than the theoretical copper content in the θ-Al_2Cu phase. However, it could be assumed that these grains corresponded to θ-Al_2Cu phase and the error in the chemical composition was attributed to the limited resolution of EDS analyses. The Al–Cu columnar grains, located at the outer part of the deposit (in contact with the electrolyte), appeared uniform in composition with an average copper content of about 2.7 at.%. This copper content is significantly higher to that corresponding to the α-solid solution (indeed, the solubility of copper in aluminium at room temperature is only 0.02 at.%) but this result is in agreement with previous works which showed that PVD process led to a supersaturated α-solution [25,27]. Besides, the experimental crystallographic data obtained from the diffraction pattern performed at the centre layer i.e., out of the equiaxed grains, confirmed the α-Al structure. An example is presented in Fig. 2b using the CaRIne Cristallographie software. The *d*-spacings calculated for several grains with a good reproducibility, and corresponding to the following crystal plane directions [111], [200] and [202] allowed the crystal lattice parameters to be calculated for the model alloys, respectively equal to 0.407, 0.400, and 0.404 nm. These values were close to the theoretical value of 0.405 nm for the fcc aluminium structure. The difference between the two sets of values i.e. the experimental crystal lattice parameter and the theoretical ones showed that the columnar grains could be considered to correspond to the α-Al supersaturated solid solution. As a conclusion, since the copper content of the columnar grains was close to that of the AA2024 matrix (Table 3), it was assumed that the Al–Cu alloy was representative of the AA2024 matrix.

Table 1
Aluminium and copper contents of the Al–Cu model alloy for equiaxed grains (points 1–5) reported in Fig. 2a.

at.%	1	2	3	4	5	Mean value	Standard deviation
Al	75.7	79.8	73.7	76.4	75.5	76.2	2.0
Cu	24.3	20.2	26.3	23.6	24.5	23.8	2.0

Fig. 3 shows a TEM micrograph of the Al–Cu–Mg alloy (Fig. 3a) and the corresponding electron diffraction pattern (Fig. 3b). Similar to the sputtered Al–Cu alloy, the Al–Cu–Mg alloy appeared uniform in thickness (about 650 nm thick) and free of defects. Unlike the binary alloy, the ternary alloy displayed an amorphous structure, confirmed by the electron diffraction (Fig. 3b). This is a classical result for ternary Al–Cu–Mg alloys deposited by magnetron sputtering. Blanc et al. [25] studied the corrosion behaviour of such alloys. They have not attributed the amorphous structure to the high alloying element content but to the third alloying element (magnesium) in significant amounts. The authors assumed that the crystallographic structure of such model alloys is not as significant as the chemical composition. Indeed, in spite of the amorphous structure, the sputtered Al–Cu–Mg alloy was shown to be representative of the corrosion behaviour of the 2024 alloy in sulphate solutions and in the cathodic range [25]. As for the latter, Liu et al. [20,31] revealed that such model alloys were electrochemically representative of the S second phase (Al_2CuMg) particles present in the AA2024 alloy. The chemical composition of the ternary alloy does not resemble that of any bulk alloys. Bulk Al–Cu–Mg model alloys have a microstructure very different from AA2024 S-phase particles since they are generally multiphase [12]. PVD model alloys are difficult to obtain with a homogeneous and reproducible composition. However, unlike bulk alloys, the present ternary alloy was shown to be monophase and with the exact composition of the S-phase particles present in the 2024 aluminium alloy. Indeed, EDS analyses at the nine numbered locations are presented in Table 4; a uniform composition of Al–22.4 at.%Cu–24.2 at.%Mg was revealed for the nine analyses, which confirms that the deposited alloy is chemically representative of the S-Al_2CuMg phase.

3.2. Corrosion behaviour of the individual model alloys

Fig. 4 shows the polarisation curves for the Al–Cu and Al–Cu–Mg alloys in 10^{-1} M Na_2SO_4 electrolyte. The polarisation curve of pure aluminium and AA2024 alloy in the same electrolyte are also reported for comparison. All the polarisation curves exhibit a cathodic current plateau corresponding to the oxygen reduction reaction (ORR). Results show that the ORR plateau is higher for the Al–Cu, Al–Cu–Mg and AA2024 alloys than for pure aluminium which could be related to enhanced kinetics of the ORR on copper

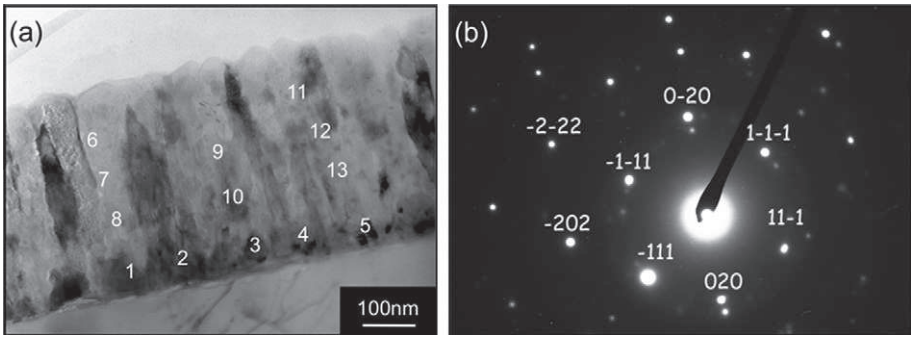

Fig. 2. (a) TEM micrograph of the Al–Cu model alloy and (b) electron diffraction pattern realised on one of the columnar grains in the [101] zone axis.

Table 2
Aluminium and copper contents of the Al–Cu model alloy for columnar grains (points 6–13) reported in Fig. 2a.

at.%	6	7	8	9	10	11	12	13	Mean value	Standard deviation
Al	97.1	97.7	97.2	96.7	97.9	96.9	97.9	97.7	97.4	0.4
Cu	2.9	2.3	2.8	3.3	2.1	3.1	2.1	2.3	2.6	0.4

Table 3
Chemical composition of the 2024 aluminium alloy.

Elements	Al	Cu	Mg	Mn	Fe	Si
wt.%	Base	3.8–4.9	1.2–1.8	0.3–0.9	⩽0.5	⩽0.5

in comparison to the kinetics on aluminium. Comparison of the cathodic current density for Al–Cu–Mg alloy to that for Al–Cu alloy confirms this result since the higher copper content in the model alloy the higher the cathodic current density. Results confirm the corrosion mechanisms proposed on the AA2024 alloy [10,12,18]: the ORR takes place preferentially on the copper-rich intermetallic particles such as S-Al_2CuMg phase particles and leads to the local alkalinisation of the medium and provokes the depassivation of the aluminium matrix around the particles, which is characterised by a trenching of the surrounding matrix. Concerning the anodic domain, it presents, for the Al–Cu alloy, a passive region plateau, which superimposes with that for pure aluminium, with current densities values of about 10^{-6} A/cm^2. On the contrary, the anodic domain for Al–Cu–Mg alloy presents a current peak (−300 mV/MSE) followed by a passive region. Optical microscopy observations before and after the current peak in the 10^{-1} M Na_2SO_4 electrolyte showed that it may be attributed to local dissolution phenomena and subsequent repassivation of the Al–Cu–Mg alloy. Indeed, as shown by Mankowski et al. [32], sulphate ions can be responsible for pitting corrosion of copper.

A similar current peak (at the same potential of about −300 mV/MSE) had been observed previously for the AA2024 alloy in chloride-containing nitrate solution [9], which was attributed to S-phase particle dissolution. In the present study, such an anodic peak was not observed for AA2024 in sulphate solutions and only a passive plateau was recorded. It could thus be concluded that, in sulphate solutions, AA2024 is passive and breakdown of the passivity could locally appear on S-phase particles. However, here, the anodic currents corresponding to the dissolution of S-phase in AA2024 do not lead to a passivity breakdown: they are either too low or the dissolution of S-phase occurred during the cathodic polarisation.

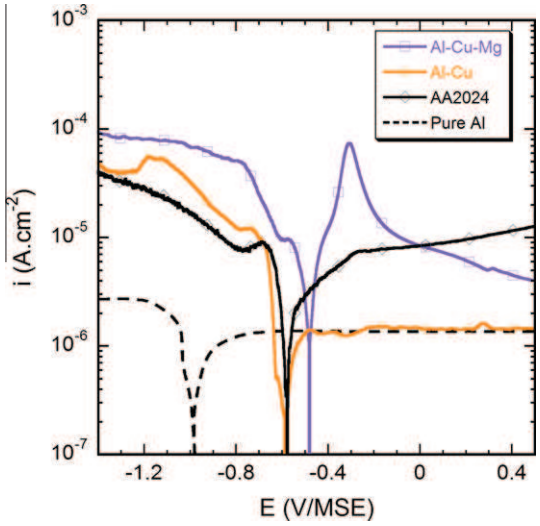

Fig. 4. Polarisation curves of Al–Cu and Al–Cu–Mg model alloy in a 10^{-1} M Na_2SO_4 solution. The polarisation curves of pure aluminium and AA2024 alloy in a 10^{-1} M Na_2SO_4 solution were reported for comparison. Potential scan rate v_b = 1 V/h.

3.3. Corrosion behaviour of the couple: LEIS measurements

Open circuit potential (OCP) measurements were performed initially to determine the time necessary for the potential to

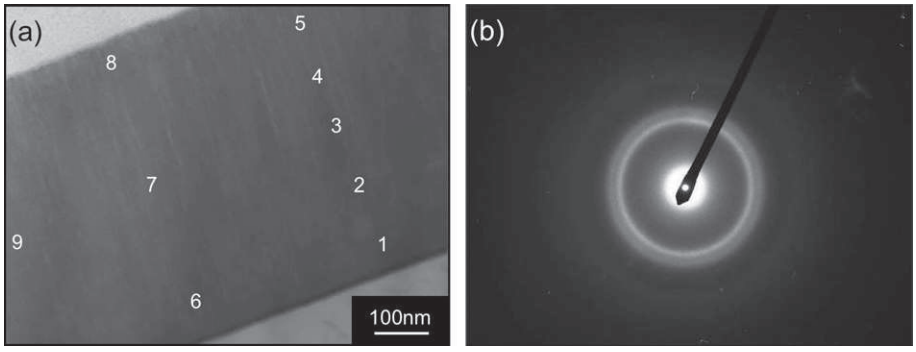

Fig. 3. (a) TEM micrograph and (b) electron diffraction pattern of Al–Cu–Mg model alloy and (b) electron diffraction pattern realised on one of the point of the layer.

Table 4
Aluminium, copper and magnesium contents of the Al–Cu–Mg model alloy for the points reported in Fig. 3a.

at.%	1	2	3	4	5	6	7	8	9	Mean value	Standard deviation
Al	53.4	52.5	53.2	51.9	53.1	55.6	54	53.2	54.3	53.5	1.0
Cu	21.1	22.7	23	24.6	25.1	18.5	21.8	23.3	21.3	22.4	1.9
Mg	25.5	24.8	23.8	23.5	21.8	25.9	24.2	23.5	24.4	24.2	1.1

stabilise before undertaking LEIS measurements. Fig. 5 presents the variation of OCP with time for the individual Al–Cu and Al–Cu–Mg alloys, and the Al–Cu/Al–Cu–Mg couple. The OCPs of the individual Al–Cu and Al–Cu–Mg alloys displayed marked changes over the initial immersion periods (150 min). Subsequently, both OCPs stabilised with values around −0.8 V/MSE for the Al–Cu alloy and −0.4 V/MSE for the Al–Cu–Mg alloy. Interestingly, during the first 100 min of immersion (dotted vertical line in Fig. 5), the OCP of the Al–Cu alloy was more positive than that for the Al–Cu–Mg alloy (*Step 1*) whereas, after immersion for 100 min, the OCP of the Al–Cu alloy was more negative than that for the Al–Cu–Mg alloy (*Step 2*). The OCP of the model couple increased rapidly from −1.8 to −0.7 V/MSE at the beginning of immersion then stabilised after 60 min.

After OCP stabilisation, local electrochemical impedance spectroscopy was performed for different positions on the model couple. Fig. 6 shows a schematic representation of the model couple electrode with the position of the probe for the local impedance measurements. The *x*-axis origin corresponds to the interface between Al–Cu–Mg (negative values) and Al–Cu (positive values) alloy parts. Electrochemical impedance measurements were performed for short immersion times (after 60 min of immersion in the electrolyte) and for long immersion times (after 600 min of immersion in the electrolyte). It is worthy noticing that, for short immersion time, Al–Cu is cathodically polarised in the model couple while, for long immersion times (600 min for example), Al–Cu is anodically polarised. Moreover, 60 min corresponds to the stabilisation of the couple OCP (Fig. 5). Fig. 7 shows the local electrochemical impedance spectra obtained on the Al–Cu–Mg alloy part (Fig. 7a) and Al–Cu alloy part (Fig. 7b), after immersion for 60 min in the 10^{-3} M Na2SO4 solution while the corresponding impedance spectra obtained after immersion for 600 min are given respectively in Fig. 7c and d. The spectra of the individual Al–Cu–Mg (Fig. 7a and c) and Al–Cu (Fig. 7b and d) alloys were reported for comparison. These spectra were plotted after 150 min of immersion, which corresponds in the stabilisation of the OCP values of the individual model alloys. For short immersion times, the spectra of the Al–Cu–Mg part (Fig. 7a) present an inductive loop and a capacitive loop. The size of the inductive loop is greatest near the interface of the Al–Cu–Mg/Al–Cu alloy and then decreases as the distance from the interface increases. This is related to the geometrical effect due to the equipotential line distribution over the surface of an embedded electrode, [33–36]. The local impedance spectrum of the individual Al–Cu–Mg alloy shows slightly lower impedance values than those of the Al–Cu–Mg alloy part of the couple. Observations of the Al–Cu–Mg alloy electrode surface had revealed pitting corrosion during the initial period of immersion, in agreement with the low impedance values measured on this alloy material. The local impedance spectra of the Al–Cu alloy part (Fig. 7b and d) shows, for the position close to the interface ($x = +1$), a capacitive behaviour with two time constants ascribed to the oxygen reduction reaction (charge transfer process and semi-infinite diffusion). This is in accordance with the polarisation of the model couple for short immersion times with Al–Cu which acts as a cathode. When the measurements are performed far from the interface ($x = +4$), the impedance response is similar to that of individual Al–Cu alloy. Such a behaviour corresponds to the galvanic coupling effect between both alloys. Comparison of Fig. 7a and b reveals that the impedance values at low frequencies are higher (1.5 decades) on the Al–Cu alloy part than on the Al–Cu–Mg alloy part, revealing the capacitive behaviour of the Al–Cu alloy and the reactive behaviour of the Al–Cu–Mg alloy when both are coupled. No passivation of the latter alloy was observed and, conversely, dissolution phenomena have been identified. These results are in agreement with the polarisation curves plotted for each individual model alloy (Fig. 4). A current peak is present in the anodic part of the polarisation curve of the Al–Cu–Mg alloy revealing dissolution phenomena and a passive plateau on the polarisation curve of the Al–Cu alloy. For long immersion times, the impedance spectra plotted for Al–Cu–Mg model alloy showed that there was a decrease of the impedance when the immersion time increased. This showed that, despite of the inversion of the polarisation of the model couple (Fig. 5), corrosion phenomena went on occurring on Al–Cu–Mg alloy. For Al–Cu alloy, a strong capacitive behaviour was observed for long immersion times in agreement with the inversion of the polarisation of the model couple: Al–Cu model alloy became the anode of the couple and remained passive as shown by the polarisation curve plotted for individual Al–Cu model alloy (Fig. 4).

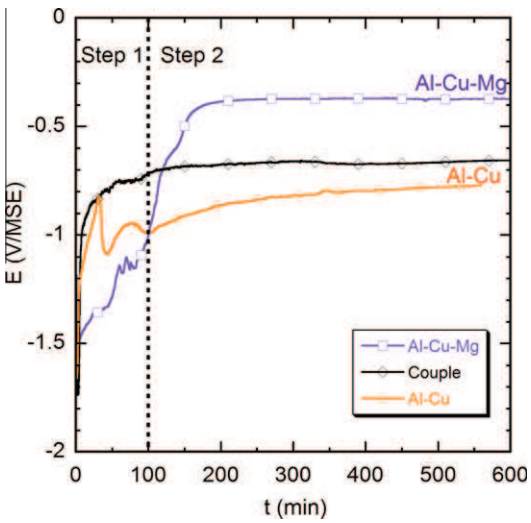

Fig. 5. Open circuit potentials of Al–Cu alloy, Al–Cu–Mg alloy and the couple in a 10^{-3} M Na_2SO_4 solution. The dotted vertical line indicates the transition between Step 1 (short immersion times) and Step 2 (long immersion times).

Results thus showed that, when the two alloys were coupled, the Al–Cu alloy part was polarised cathodically during the first 100 min (*Step 1*), with the Al–Cu–Mg alloy part being the anode. Some pits may be formed on the Al–Cu–Mg alloy, which explained the low impedance values obtained for this alloy after immersion for 60 min. After immersion for 100 min, (*Step 2*) the corrosion potentials of the two individual materials were reversed (Fig. 5). Thus, the Al–Cu alloy became the anode of the system and passivated, since it did not develop any pits in the sulphate medium as shown on the current–potential curves. The Al–Cu–Mg alloy became the cathode of the system. It was assumed that, even if this alloy was the preferred site for the oxygen reduction reaction, the anodic component on it was significant, particularly with local dissolution phenomena. Further, these alloys are covered by a passive layer at the corrosion potential at the commencement of immersion. Even though galvanic coupling occurs and oxygen reduction on copper-rich parts then leads to a rapid depassivation of the zones due to subsequent alkalinisation. Such corrosion phenomena may be combined with changes in surface chemistry of the alloys, which could also explain the potential variations with time (Fig. 5). Optical microscopy observations and SEM characterisation combined with EDS analyses were conducted to characterise the corrosion damage and check the assumptions made previously about the electrochemical behaviour of both alloys in the couple.

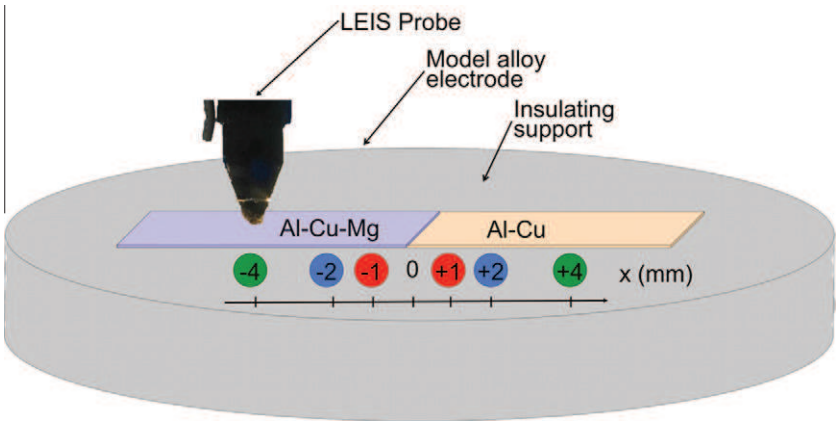

Fig. 6. Schematic representation of the different LEIS measurement locations on a model alloy electrode. The distance values are given in millimetres.

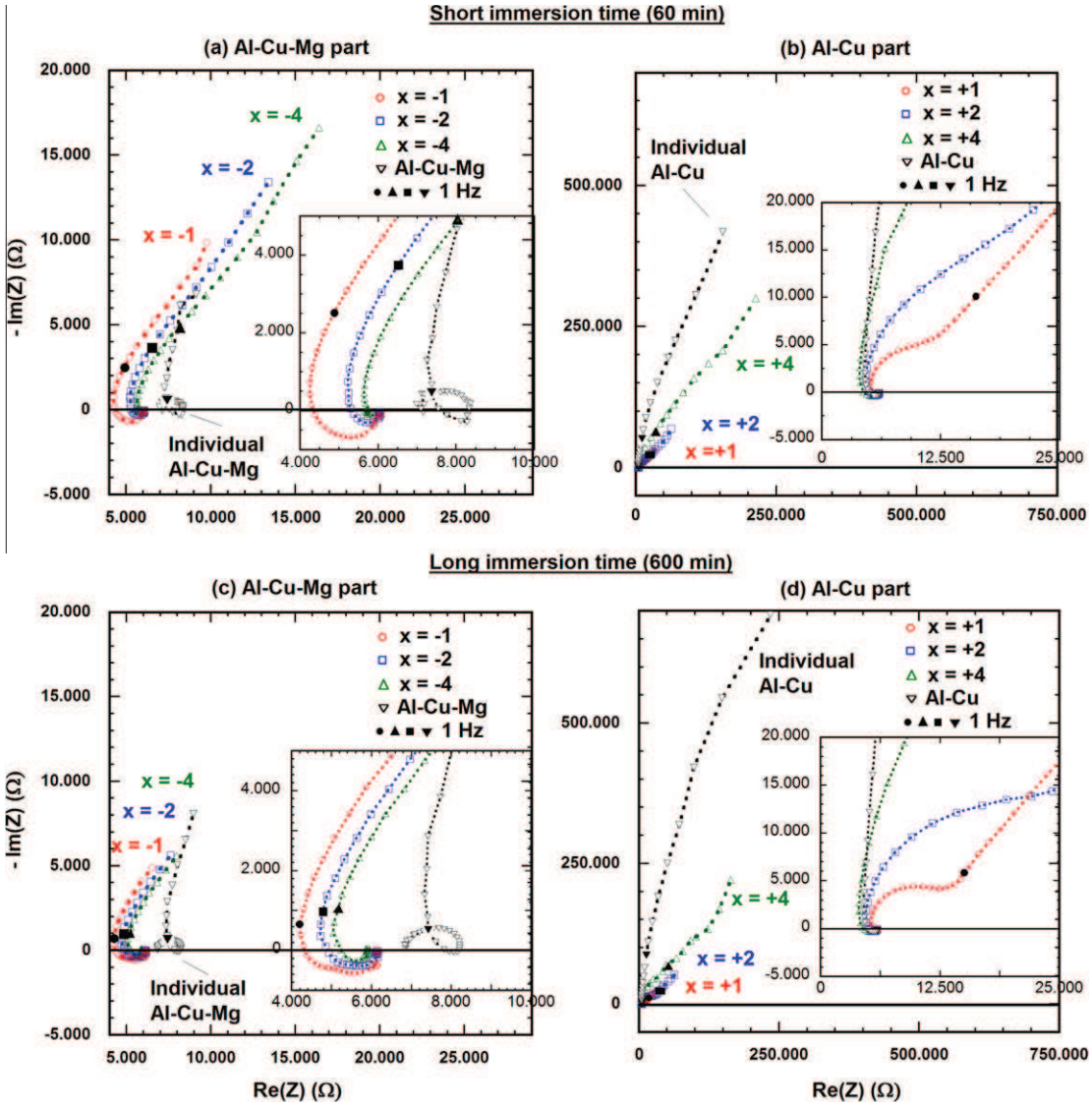

Fig. 7. LEIS spectra in Nyquist representation above (a and c) the Al–Cu–Mg alloy part and (b and d) the Al–Cu alloy part of the couple after short immersion time (60 min) and long immersion time (600 min) in a 10^{-3} M Na_2SO_4 solution. An inset, representing a magnification of the spectra in the high-frequency range was added in each graph. LEIS spectra of individual Al–Cu–Mg and Al–Cu alloy were reported for comparison, for short immersion time (150 min) and long immersion time (600 min).

3.4. Microscopic observations and chemical analysis of the corrosion damage

Fig. 8 shows a photograph (Fig. 8a) and the corresponding optical micrograph (Fig. 8b) of the model alloy couple after immersion for 60 min in the 10^{-3} M Na_2SO_4 solution. The couple after immersion for 600 min is presented in Fig. 8c, with magnified images on each part of the couple displayed in Figs. 8d and e. The large differences in reflectivity on both parts of the couple did not allow the simultaneous observation of both parts. Indeed the Al–Cu–Mg alloy part appeared corroded while the Al–Cu alloy part appeared almost intact (Fig. 8b). Interestingly, the Al–Cu–Mg alloy part was more corroded close to the interface, revealing the galvanic coupling effect. As explained before, sulphate ions are responsible for pitting corrosion [32], which is enhanced at locations of higher galvanic currents, i.e., at the interface between both model alloys. After 600 min, the Al–Cu–Mg alloy part appeared severely corroded compared with the Al–Cu alloy part. Further, many similarly sized pits (about 100 μm in diameter) were present on the Al–Cu–Mg alloy whereas, except for some small pits (about 10 μm in diameter) that are probably unstable, the Al–Cu alloy appeared passive. These observations were fully consistent with the assumptions made earlier after the analysis of local impedance measurements of the couple and the current–voltage curves for the individual alloys.

In order to further characterise the phenomena occurring on the Al–Cu–Mg alloy, chemical analyses were performed. Fig. 9 shows optical (Fig. 9a) and SEM (Fig. 9b) micrographs of the Al–Cu–Mg alloy part presented in Fig. 8 after immersion for 600 min in 10^{-3} M Na_2SO_4 solution. EDS spectra performed on the previous corroded sample are shown in Fig. 8c. Spectra analysis locations are marked in Fig. 9b from N°1 (far from the pit) to N°4 (in the pit).

Spectrum N°0 corresponds to analysis performed on the Al–Cu–Mg alloy before immersion. No significant composition differences were observed between spectrum N°1 and spectrum N°0; far from the pit, the Al–Cu–Mg alloy composition did not change after immersion for 600 min. Further, EDS spectra revealed a gradual variation of the chemical composition from the S-phase composition (N°1) to a composition almost exclusively copper and oxygen (N°4). Indeed, it is revealed that the aluminium and magnesium contents decreased from spectrum N°1 to spectrum N°4. For spectrum N°4, the magnesium peak was absent and the aluminium peak was very low. The chemical analysis thus showed that the Al–Cu–Mg alloy had undergone preferential dissolution of aluminium and magnesium in the vicinity of the pit, leading to a strong copper enrichment. This behaviour is consistent with the phenomena presented to explain S-phase particle reactivity in the AA2024 alloy. A schematic diagram of the corrosion behaviour of the model couple is presented in Fig. 10. In the initial state, both Al–Cu–Mg and Al–Cu parts are passivated (Fig. 10a). During immersion, because of the presence of magnesium, the Al–Cu–Mg alloy had a more cathodic potential than the Al–Cu alloy. In the couple, the Al–Cu–Mg alloy part was anodically polarised and localised corrosion phenomena occurred, leading to a preferential dissolution of aluminium and magnesium, which corresponds to the first step of the diagram (Fig. 10b). This first step resulted in a strong copper enrichment. The chemical composition change could explain the observed reversal of the corrosion potentials of the two model alloys. In the couple, after immersion for 100 min (*Step 2*), the Al–Cu alloy became the anode of the system, but it remained passive in

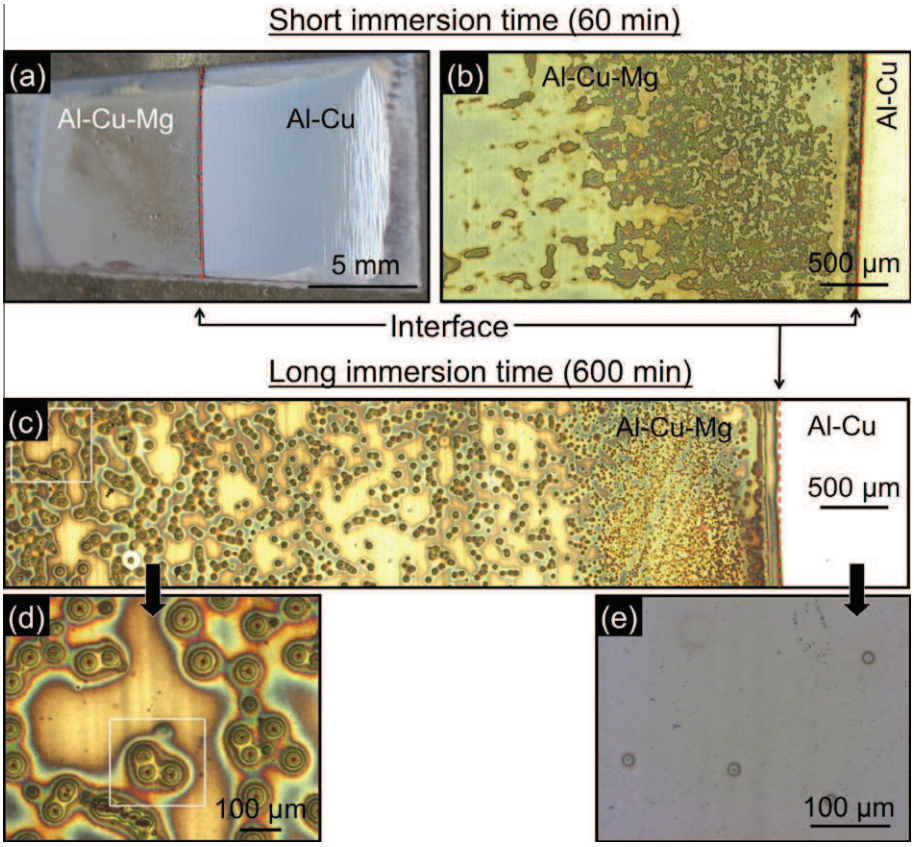

Fig. 8. Photograph and optical micrographs of the couple interface after (a and b) 60 min and (c–e) 600 min of immersion in 10^{-3} M Na_2SO_4 solution. Magnification on each part of the couple after 600 min of immersion (d and e).

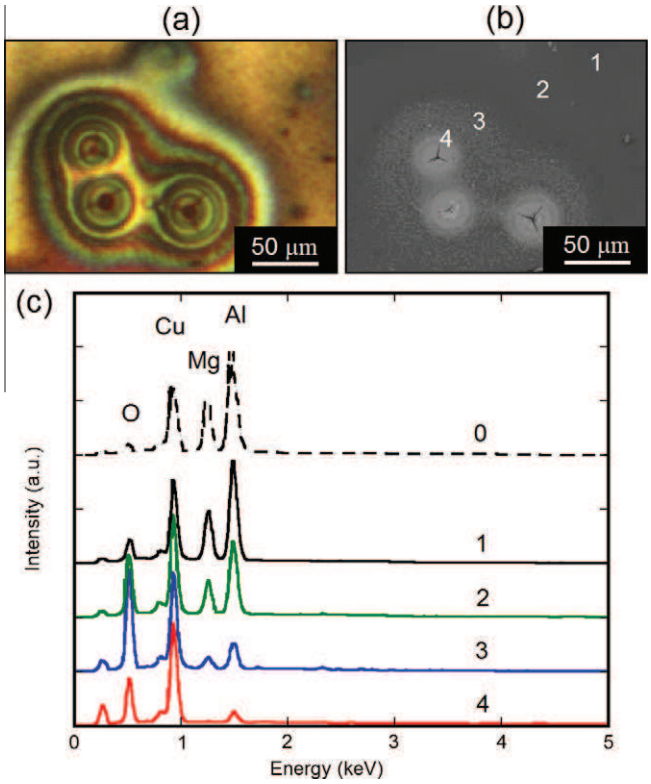

Fig. 9. (a) Optical and (b) SEM micrograph of the framed pits of the Fig. 8c and d. (c) EDS spectra at different distances from a pit (point marked 1–4 in b). The spectra N°0 was performed on the Al–Cu–Mg alloy before immersion.

the sulphate medium (Fig. 10c). However, it was assumed that the pits continued to grow on the Al–Cu–Mg alloy. In Fig. 8, the Al–Cu–Mg alloy appeared more damaged at the interface with the Al–Cu alloy part. These observations can be correlated with the changes observed with the probe position for the impedance spectra performed on the Al–Cu–Mg alloy part of the couple after immersion for 90 min in sulphate medium. Indeed, the gradual reduction of the magnitude of the high frequency inductive loop with distance from the interface had been observed before (Fig. 7). These observations are a sign of the galvanic coupling phenomenon.

4. Conclusions

As a prerequisite for the simulation of the galvanic coupling, the individual Al–Cu and Al–Cu–Mg model alloys were shown to be representative of the corrosion behaviour of the AA2024 alloy. Anodic and cathodic current densities measured on the Al–Cu–Mg alloy were about ten times higher than those on the Al–Cu alloy; this was attributed to the high copper content of the Al–Cu–Mg alloy. Thereby, the high copper content increased susceptibility of the Al–Cu–Mg alloy to pitting corrosion due to the presence of sulphate ions. An anodic current peak was observed on the Al–Cu–Mg alloy polarisation curve. This current peak was attributed to dissolution phenomena, which are totally representative of the dissolution of the S-phase particles of the AA2024 alloy.

LEIS showed a capacitive behaviour of the Al–Cu alloy part of the couple while the Al–Cu–Mg alloy part appeared to be the location of strong reactivity. While the Al–Cu alloy part remained in a passive state, the Al–Cu–Mg alloy part underwent significant localised corrosion. The preferential dissolution of magnesium observed

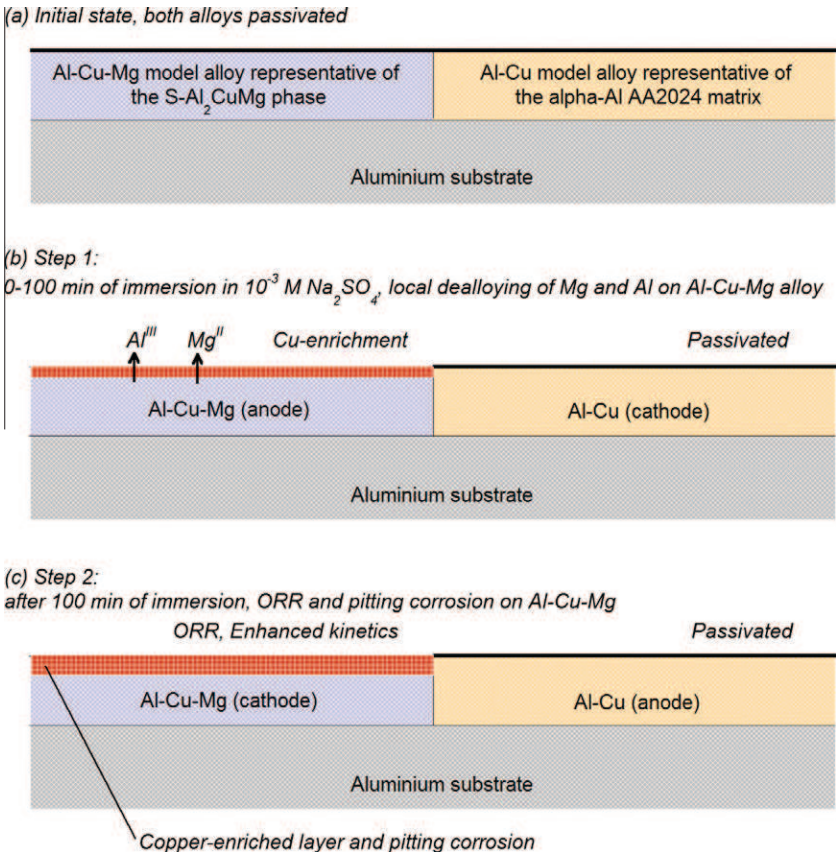

Fig. 10. Schematic diagram of the corrosion behaviour of the model couple alloy, (a) initial state, (b) Step 1, up to 100 min of immersion in 10^{-3} M Na_2SO_4 and (c) Step 2, after 100 min of immersion.

in the commercial AA2024 alloy was highlighted in the magnetron sputtered couple model alloy.

The results showed that model couples constitute an original and efficient approach to study corrosion mechanisms involving galvanic coupling. The study of model alloys used to simulate events highlighted on the commercial AA2024 alloy was relevant, although the thin nature of the sputtered layers may limit long term testing. The macroscopic model systems (centimetre scale), studied by stationary and transient electrochemical methods, were shown to be representative of submicron phenomena that occur on the intermetallic particles of the commercial AA2024 alloy.

Acknowledgements

The authors thank Mirnali Saenz and Peter Skeldon for their help in the PVD model alloy deposition and the support of the EPSTRC LATEST2 Programme Grant.

References

[1] J.W.J. Silva, A.G. Bustamante, E.N. Codaro, R.Z. Nakazato, L.R.O. Hein, Morphological analysis of pits formed on Al 2024-T3 in chloride aqueous solution, Appl. Surf. Sci. 236 (2004) 356–365.
[2] A. Garner, D. Tromans, Direct observation of intergranular corrosion in Al–4 wt%Cu alloy, Corrosion 35 (1979) 55–60.
[3] X. Zhao, G.S. Frankel, B. Zoofan, S.I. Rokhlin, In situ X-ray radiographic study of intergranular corrosion in aluminum alloys, Corrosion 59 (2003) 1012–1018.
[4] X. Liu, G.S. Frankel, B. Zoofan, S. Rokhlin, In-situ observation of intergranular stress corrosion cracking in AA2024-T3 under constant load conditions, Corros. Sci. 49 (2007) 139–148.
[5] J.F. Li, Z. Ziqiao, J. Na, T. Chengyu, Localized corrosion mechanism of 2×××-series Al alloy containing S(Al_2CuMg) and θ′(Al_2Cu) precipitates in 4.0% NaCl solution at pH 6.1, Mater. Chem. Phys. 91 (2005) 325–329.
[6] V. Guillaumin, G. Mankowski, Localized corrosion of 2024 T351 aluminium alloy in chloride media, Corros. Sci. 41 (1998) 421–438.
[7] W. Zhang, G.S. Frankel, Transitions between pitting and intergranular corrosion in AA2024, Electrochim. Acta 48 (2003) 1193–1210.
[8] C. Blanc, B. Lavelle, G. Mankowski, The role of precipitates enriched with copper on the susceptibility to pitting corrosion of the 2024 aluminium alloy, Corros. Sci. 39 (1997) 495–510.
[9] C. Blanc, S. Gastaud, G. Mankowski, Mechanistic studies of the corrosion of 2024 aluminum alloy in nitrate solutions, J. Electrochem. Soc. 150 (2003) B396–B404.
[10] R.G. Buchheit, R.P. Grant, P.F. Hlava, B. McKenzie, G.L. Zender, Local dissolution phenomena associated with S phase (Al[sub 2]CuMg) particles in aluminum alloy 2024-T3, J. Electrochem. Soc. 144 (1997) 2621–2628.
[11] R.G. Buccheit, M.A. Martinez, L.P. Montes, Evidence for Cu ion formation by dissolution and dealloying the Al_2CuMg intermetallic compound in rotating ring-disk collection experiments, J. Electrochem. Soc. 147 (2000) 119–124.
[12] R.G. Buchheit, L.P. Montes, M.A. Martinez, J. Michael, P.F. Hlava, The electrochemical characteristics of bulk-synthesized Al_2CuMg, J. Electrochem. Soc. 146 (1999) 4424–4428.
[13] A. Hughes, T.H. Muster, A. Boag, A.M. Glenn, C. Luo, X. Zhou, G.E. Thompson, D. McCulloch, Co-operative corrosion phenomena, Corros. Sci. 52 (2010) 665–668.
[14] T. Suter, R.C. Alkire, Microelectrochemical studies of pit initiation at single inclusions in Al 2024-T3, J. Electrochem. Soc. 148 (2001) B36–B42.
[15] M. Shao, Y. Fu, R. Hu, C. Lin, A study on pitting corrosion of aluminum alloy 2024-T3 by scanning microreference electrode technique, Mater. Sci. Eng. A 344 (2003) 323–327.
[16] P. Schmutz, G.S. Frankel, Characterization of AA2024-T3 by scanning Kelvin probe force microscopy, J. Electrochem. Soc. 145 (1998) 2285–2295.
[17] L. Lacroix, L. Ressier, C. Blanc, G. Mankowski, Statistical study of the corrosion behavior of Al_2CuMg intermetallics in AA2024-T351 by SKPFM, J. Electrochem. Soc. 155 (2008) C8–C15.
[18] L. Lacroix, L. Ressier, C. Blanc, G. Mankowski, Combination of AFM, SKPFM, and SIMS to study the corrosion behavior of S-phase particles in AA2024-T351, J. Electrochem. Soc. 155 (2008) C131–C137.
[19] J. Idrac, C. Blanc, Y. Kihn, M.C. Lafont, G. Mankowski, P. Skeldon, G.E. Thompson, Electrochemical behavior of magnetron-sputtered Al–Cu alloy films in sulfate solutions, J. Electrochem. Soc. 154 (2007) C286–C293.
[20] Y. Liu, E.A. Sultan, E.V. Koroleva, P. Skeldon, G.E. Thompson, X. Zhou, K. Shimizu, H. Habazaki, Grain orientation effects on copper enrichment and oxygen generation during anodizing of an Al–1 at.%Cu alloy, Corros. Sci. 45 (2003) 789–797.
[21] S. Garcia-Vergara, P. Skeldon, G.E. Thompson, P. Bailey, T.C.Q. Noakes, H. Habazaki, K. Shimizu, Morphology of enriched alloy layers in an anodized Al–Cu alloy, Appl. Surf. Sci. 205 (2003) 121–127.
[22] M.B. Vukmirovic, N. Dimitrov, K. Sieradzki, Dealloying and Corrosion of Al Alloy 2024-T3, J. Electrochem. Soc. 149 (2002) B428–B439.
[23] J.B. Jorcin, C. Blanc, N. Pébère, B. Tribollet, V. Vivier, Galvanic coupling between pure copper and pure aluminum, J. Electrochem. Soc. 155 (2008) C46–C51.
[24] L. Lacroix, C. Blanc, N. Pébère, B. Tribollet, V. Vivier, Localized approach to galvanic coupling in an aluminum–magnesium system, J. Electrochem. Soc. 156 (2009) C259–C265.
[25] C. Blanc, A. Freulon, M.C. Lafont, Y. Kihn, G. Mankowski, Modelling the corrosion behaviour of Al_2CuMg coarse particles in copper-rich aluminium alloys, Corros. Sci. 48 (2006) 3838–3851.
[26] M. Saenz de Miera, M. Curioni, P. Skeldon, G.E. Thompson, Modelling the anodizing behaviour of aluminium alloys in sulphuric acid through alloy analogues, Corros. Sci. 50 (2008) 3410–3415.
[27] J. Idrac, G. Mankowski, G.E. Thompson, P. Skeldon, Y. Kihn, C. Blanc, Galvanic corrosion of aluminium–copper model alloys, Electrochim. Acta 52 (2007) 7626–7633.
[28] G. Baril, C. Blanc, M. Keddam, N. Pébère, Local electrochemical impedance spectroscopy applied to the corrosion behavior of an AZ91 magnesium alloy, J. Electrochem. Soc. 150 (2003) B488–B493.
[29] J.B. Jorcin, E. Aragon, C. Merlatti, N. Pébère, Delaminated areas beneath organic coating: a local electrochemical impedance approach, Corros. Sci. 48 (2006) 1779–1790.
[30] J.B. Jorcin, M.E. Orazem, N. Pébère, B. Tribollet, CPE analysis by local electrochemical impedance spectroscopy, Electrochim. Acta 51 (2006) 1473–1479.
[31] Y. Liu, M.A. Arenas, P. Skeldon, G.E. Thompson, P. Bailey, T.C.Q. Noakes, H. Habazaki, K. Shimizu, Anodic behaviour of a model second phase: Al–20 at.%Mg–20 at.%Cu, Corros. Sci. 48 (2006) 1225–1248.
[32] G. Mankowski, J.P. Duthil, A. Giusti, The pit morphology on copper in chloride- and sulphate-containing solutions, Corros. Sci. 39 (1997) 27–42.
[33] I. Frateur, V.M.-W. Huang, M.E. Orazem, B. Tribollet, V. Vivier, Experimental issues associated with measurement of local electrochemical impedance, J. Electrochem. Soc. 154 (2007) C719–C727.
[34] C. Blanc, M.E. Orazem, N. Pébère, B. Tribollet, V. Vivier, S. Wu, The origin of the complex character of the Ohmic impedance, Electrochim. Acta 55 (2010) 6313–6321.
[35] V.M.-W. Huang, V. Vivier, I. Frateur, M.E. Orazem, B. Tribollet, The apparent constant-phase-element behavior of a disk electrode with Faradaic reactions, J. Electrochem. Soc. 154 (2007) C99–C107.
[36] V.M.-W. Huang, S.-L. Wu, M.E. Orazem, N. Pébère, B. Tribollet, V. Vivier, Local electrochemical impedance spectroscopy: a review and some recent developments, Electrochim. Acta 56 (2011) 8048–8057.